JOURNAL OF AIRCRAFT
Vol. 29, No. 3, May-June 1992

Numerical Study of Vortex-Dominated Flows for Wings at High Incidence and Sideslip

C.-H. Hsu*
ViGYAN, Inc., Hampton, Virginia 23666
and
C. H. Liu†
NASA Langley Research Center, Hampton, Virginia 23665

Three-dimensional viscous flows past a double-delta wing and a delta wing are numerically investigated. A computational method for calculating low-speed viscous flowfields is discussed. The time-iterative method uses an implicit upwind-relaxation finite difference algorithm with a nonsingular eigensystem to solve the preconditioned, three-dimensional, incompressible Navier-Stokes equations in curvilinear coordinates. An algebraic turbulence model is implemented to account for the eddy viscosity. The technique of local time stepping is incorporated to accelerate the rate of convergence to a steady-state solution. Computed results are compared with experimental data.

Introduction

THIN, slender, and highly swept wings are of increasing importance for many modern aircraft. The flow about these wings at high angles of attack (α) is dominated by leading-edge separation vortices which provide useful vortical lift. At high α flight conditions such as takeoff, landing, and supermaneuvering, the effect of sideslip (β) can be crucial for the stability and control of aircraft.

To simulate the complicated vortical flows, a proper mathematical model is strongly needed. As a model for the prediction of three-dimensional leading-edge separation vortices, the Euler equations are fundamentally incapable of predicting boundary-layer flows or secondary separation vortices. To model correctly all relevant physical mechanisms, the Navier-Stokes equations must be solved.

In recent years, several compressible flow codes have been applied to low-Mach-number (M_∞) flows for the purpose of validating those codes against experimental data obtained in diagnostic water tunnels, towing tanks, and low-speed wind tunnels. However, most compressible flow codes become inefficient as the Mach number decreases to 0.2 or lower.[1] One of the reasons is that the disparity in the magnitude of the speed of sound and that of the flow velocity increases as the flow approaches the incompressible limit ($M_\infty = 0$). Another potential reason is that most multidimensional implicit compressible flow schemes use approximate factorization. Because of increasing factorization error, the convergence deteriorates rapidly as the Mach number decreases.[2,3]

Here, the three-dimensional incompressible Navier-Stokes equations are used. There are primarily two reasons for doing this. First, there is one less variable than that using the compressible flow equations, because the density remains constant. Second, the numerical stability limit is independent of the speed of sound.

The concept of artificial compressibility was first proposed by Chorin.[4] It is noted that the continuity equation for incompressible flows does not contain the time derivative of the velocity or pressure explicitly. Hence, in the integration of the conservation equations, the continuity equation serves as a compatibility condition to assure that the flow remains divergence-free. To solve the system of equations with a time-iterative scheme, especially an implicit upwind scheme, the continuity equation must be modified so that the whole system of equations is coupled together and solved efficiently. By adding an artificial time derivative of pressure (artificial compressibility) to the continuity equation, the elliptic-parabolic nature of the unsteady incompressible Navier-Stokes equations is changed to a hyperbolic-parabolic one. Therefore, well-developed compressible flow algorithms can be readily applied. To accelerate convergence to a steady state, one arbitrary parameter must be determined. When a steady state is approached, the effect of artificial compressibility diminishes, resulting in an incompressible solution. Several central-difference[2-6] and flux-difference upwind[7-10] schemes have implemented this approach.

Recently, Turkel suggested a preconditioned method for solving the incompressible flow equations.[1] This method introduces artificial time derivatives not only in the continuity equation but also in the momentum equation. Now, the resultant time-dependent incompressible flow equations contain two arbitrary parameters to be determined for faster convergence to a steady state. The idea is to choose these two parameters such that the disparity in wave speeds will be minimized during the unphysical transient state. In this approach, the system of equations is less directionally dependent and better numerically conditioned.

In the present paper, a nonsingular three-dimensional eigensystem is derived and incorporated in an implicit upwind-relaxation finite difference scheme. First, the effect of preconditioned parameters on numerical accuracy and convergence is examined for a double-delta wing at $\alpha = 12$ deg. Second, the computed results of the flow over a sideslipping delta wing at $\alpha = 21$ deg are discussed.

Numerical Algorithm

Preconditioned Equations

The complete three-dimensional Navier-Stokes equations for source-free, isothermal, and constant-density fluids are

---

Presented as Paper 90-3001 at the AIAA 8th Applied Aerodynamics Conference, Portland, OR, Aug. 20-22, 1990; received Oct. 6, 1990; revision received May 6, 1991; accepted for publication May 9, 1991.

*Research Scientist. Senior Member AIAA.

†Senior Research Scientist, Theoretical Flow Physics Branch, Fluid Mechanics Division. Senior Member AIAA.

modified to the following set of equations:

$$\frac{1}{\sigma}\frac{\partial p}{\partial t} + \frac{\partial u_i}{\partial x_i} = 0$$

$$\frac{(\gamma + 1)}{\sigma} u_i \frac{\partial p}{\partial t} + \frac{\partial u_i}{\partial t} + \frac{\partial u_i u_j}{\partial x_j} = -\frac{\partial p}{\partial x_i} + \frac{\partial \tau_{ij}}{\partial x_j} \tag{1}$$

$$\tau_{ij} = \frac{1}{Re}\left(\frac{\partial u_i}{\partial x_j} + \frac{\partial u_j}{\partial x_i}\right); \quad i = 1, 2, 3; \quad j = 1, 2, 3$$

where $u_i = u, v, w$ and τ_{ij} are the velocity vector and shear-stress tensor in Cartesian coordinates with $x_i = x, y, z$; p and t are the pressure and time, respectively; and Re is the Reynolds number based on the wing root chord c and freestream velocity V_∞. The two parameters γ and σ are introduced to precondition the Navier-Stokes equations for faster convergence to a steady state.[1] In a body-fitted, curvilinear coordinate system with $\xi_i = \xi, \eta, \zeta$, Eq. (1) is reformulated in conservation form as

$$M \frac{\partial}{\partial t} \boldsymbol{D}^* + \frac{\partial}{\partial \xi_i} (\boldsymbol{E}_i^* - \boldsymbol{\Gamma}_i^*) = \boldsymbol{0} \tag{2}$$

where the preconditioned matrix M, the pressure and velocity vector $\boldsymbol{D}^*$, the inviscid flux vector $\boldsymbol{E}^*$, and the viscous diffusion vector $\boldsymbol{\Gamma}^*$ are described by

$$M = \begin{bmatrix} \sigma^{-1} & 0 & 0 & 0 \\ \sigma^{-1}(\gamma + 1)u & 1 & 0 & 0 \\ \sigma^{-1}(\gamma + 1)v & 0 & 1 & 0 \\ \sigma^{-1}(\gamma + 1)w & 0 & 0 & 1 \end{bmatrix}$$

$$\boldsymbol{D}^* = \frac{D}{J} = \frac{1}{J}[p, u, v, w]^T$$

$$\boldsymbol{E}_i^* = \frac{1}{J}[U_i, uU_i + a_i p_i, vU_i + b_i p, wU_i + c_i p]^T$$

$$\boldsymbol{\Gamma}_i^* = \frac{1}{ReJ}\left[0, (\nabla\xi_i \cdot \nabla\xi_j)\frac{\partial u}{\partial \xi_j}, (\nabla\xi_i \cdot \nabla\xi_j)\frac{\partial v}{\partial \xi_j}, (\nabla\xi_i \cdot \nabla\xi_j)\frac{\partial w}{\partial \xi_j}\right]^T$$

Here J is the Jacobian of coordinate transformation and

$$U_i = a_i u + b_i v + c_i w$$

$$a_i = (\xi_i)_x, \; b_i = (\xi_i)_y, \; c_i = (\xi_i)_z$$

are the contravariant velocities and the metrics of transformation, respectively.

Eigensystem

The eigenvectors of modified flux Jacobians are discussed below. While the choice for the two-dimensional eigenvectors is straightforward, the choice for the three-dimensional eigenvectors has more freedom. A fairly simple three-dimensional formulation was previously proposed.[7,8] For certain values of metrics, the simple eigensystem may become singular and result in excessive truncation errors.[11] In the present paper, a generalized nonsingular three-dimensional eigensystem requiring metrics information only in the considered direction is derived for the preconditioned system of equations.

The modified inviscid-flux Jacobians are expressed as

$$A_i = M^{-1}\frac{\partial \boldsymbol{E}_i^*}{\partial \boldsymbol{D}^*}$$

$$= \begin{bmatrix} 0 & \sigma a_i & \sigma b_i & \sigma c_i \\ a_i & U_i - \gamma a_i u & -\gamma b_i u & -\gamma c_i u \\ b_i & -\gamma a_i v & U_i - \gamma b_i v & -\gamma c_i v \\ c_i & -\gamma a_i w & -\gamma b_i w & U_i - \gamma c_i w \end{bmatrix} \tag{3}$$

The eigenvalues of A_i are

$$\begin{aligned} \lambda_{1,i} &= \frac{1}{2}(1 - \gamma)U_i - S_i = \lambda_i^- \\ \lambda_{2,i} &= U_i = \lambda_i^0 \\ \lambda_{3,i} &= U_i = \lambda_i^0 \\ \lambda_{4,i} &= \frac{1}{2}(1 - \gamma)U_i + S_i = \lambda_i^+ \end{aligned} \tag{4}$$

where

$$S_i = \left\{\left[\frac{1}{2}(1 - \gamma)U_i\right]^2 + \sigma\right\}^{1/2}$$

The right R and left L eigenvectors of A_i, with all metrics normalized by $(a^2 + b^2 + c^2)^{1/2}$, are given in the Appendix.

If γ is specified, σ can be chosen to minimize the largest possible ratio of wave speeds. Optimum values of γ and σ can be derived as

$$\begin{aligned} \sigma &= \max[(2 - \gamma)u_i u_i;\, \varepsilon] \quad \text{for} \quad \gamma < 1 \\ \sigma &= \Upsilon \cdot \max[\gamma \cdot u_i u_i;\, \varepsilon] \quad \text{for} \quad \gamma \geq 1 \end{aligned} \tag{5}$$

where $\varepsilon = 0.01$ and $\Upsilon = 1.01$. The parameters, ε and Υ, are introduced in the above equation to avoid difficulties near stagnation points.[1] The value of σ is not a constant, but rather an adaptive value depending on the local flow speed.

Solution Procedure

The finite difference solutions to Eq. (2) are advanced in pseudotime using Euler-implicit time differencing. An implicit scheme is chosen to avoid a restrictive time-step size when highly refined grids are used to resolve viscous effects. Casting the equations in delta form yields steady-state solutions which are independent of the time-step size. Local time stepping (Courant number of 10) is then used to further accelerate numerical convergence. The two-time-level discretization of Eq. (2) can be written as

$$N\,\Delta\, D^n + RES(D^n) = 0 \tag{6}$$

where $D = D(p, u_i)$ and $\Delta D^n = D^{n+1} - D^n$. The operator RES gives the residual at time level n and represents the discretized spatial-derivative terms of Eq. (2). The viscous fluxes are centrally differenced with second-order accuracy. In addition to making the coefficient matrices diagonally dominant, upwind-differencing procedure eliminates the necessity to add and tune the numerical dissipation for numerical stability as in the central differencing schemes. Here, the inviscid fluxes are upwind differenced by applying Roe's flux-difference splitting procedure[12] and Yee, Warming, and Hartens' high-resolution total variation diminishing (TVD) technique.[13] TVD schemes are essentially nonlinear schemes, which switch among several difference stencils so as to highly resolve the regions of smooth solutions and to suppress spurious oscillations in the regions of rapid flow changes. The TVD flux limiters can be found in Refs. 7 and 8. The resulting scheme is up to third-order accurate in spatial differencing. Furthermore, a hybrid approach for the formulation of the operator N is chosen, which uses approximate factorization in cross planes in combination with a symmetric planar Gauss-Seidel relaxation in the third direction. This scheme with block-tridiagonal implicit factors is written as

$$\begin{aligned} &\{\hat{M} + [B^+ + S^*]_{j-1/2}\Delta_{j-1/2} \\ &\quad - [B^- + S^*]_{j+1/2}\Delta_{j+1/2}\}^n \times [\hat{M}^{-1}]^n \\ &\quad \times \{\hat{M} + [C^+ + T^*]_{k-1/2}\Delta_{k-1/2} \\ &\quad - [C^- + T^*]_{k+1/2}\Delta_{k+1/2}\}^n \times \Delta D^n \\ &\quad = -RES(D^n, D^{n+1}) \end{aligned} \tag{7}$$

with

$$\hat{M} = I/(\Delta tJ) + [A^+ + R^*]_{i-1/2} + [A^- + R^*]_{i+1/2}$$

where I is the identity matrix; $A^{\pm}$, $B^{\pm}$, and $C^{\pm}$ are the Jacobian matrices related to A_i constructed through the eigenvalue decompositions; and R^*, S^*, and T^* are the linearized coefficient matrices associated with the viscous shear fluxes. The nonlinear updating of the residual during back and forth sweeps in the third direction is indicated by $RES(D^n, D^{n+1})$ in Eq. (7). On the computational boundaries, unknown values of D^n are updated explicitly and ΔD^n are set to zero.

Initial and Boundary Conditions

On the wing surface, the no-slip condition is imposed, and the normal gradient of the pressure is assumed to vanish. Freestream conditions are specified along the outer boundaries except for the outflow boundary, where the values are computed using extrapolation. The initial conditions consist of freestream values except that the no-slip condition is applied on the wing surface.

Turbulence Modeling

The modeling of turbulent flow is an increasing concern in computational fluid dynamics. At the present time there is no turbulence model that is applicable to a rotational, off-body flow, such as a free-shear flow, an organized stable vortex, or a vortex breakdown flow. For engineering purpose the concept of eddy viscosity is usually employed to account for the effect of turbulence at high Reynolds numbers. Here, the Baldwin-Lomax[14] two-layer algebraic turbulence model with the modification suggested by Degani and Schiff[15] is used.

Numerical Results

The present computer code is fully vectorized and named VOR3DI. The central processor unit (cpu) time per grid point per iteration is about 62 μs using 32-bit word arithmetic (seven significant decimal places) on the CDC CYBER 205 vector computer at the NASA Langley Research Center. Since only steady-state Navier-Stokes solutions are discussed here, one iteration actually equals one time step. Two numerical examples using the present second-order accurate method are presented.

Double-Delta Wing

The round-edged double-delta wing was tested by Brennenstuhl and Hummel in a low-speed wind tunnel at $Re = 1.3 \times 10^6$ and $M_\infty \approx 0.1$.[16] The wing has an aspect ratio of 2.05, and the maximum thickness is 0.6% of c. It has a leading-edge kink at midchord station and has 80 deg and 60 deg sweeps for the leading edges of the strake and the main wing, respectively. All edges of the wing are rounded with radii of one-half the wing thickness.

Two H–O grids are generated solving a set of Poisson equations. The origin of the coordinate system is located at the apex of the wing. The position of the outflow boundary is varied in the range of one to three root chords away from the wing, without any discernible differences in the total pressure distributions. Therefore, in the final computations all grids extend one root chord upstream and downstream of the wing and approximately two chords radially away from the longitudinal axis of the wing. Longitudinally, there are 59 successive cross planes with 10, 39, and 10 planes upstream of the apex, on the wing, and in the wake, respectively. In each cross plane the fine (coarse) grid has 97 (65) and 167 (65) mesh points in the radial (leading away from the wing surface) and circumferential directions, respectively. The detailed grids can be found in Refs. 17 and 18.

Steady-state laminar solutions for this wing are obtained at $Re = 1.3 \times 10^6$ and $\alpha = 12$ deg. Since the flowfield is symmetric with respect to the longitudinal plane of symmetry (root-chord plane), only the flowfield over half of the wing is computed. Reflection conditions are then applied on the plane of symmetry.

For the double-delta wing, it is found out that the steady-state solution is hardly obtained outside the range of $\gamma = -2 \sim 0$. Also, within the range of $\sigma = 0.1 \sim 10.0$ the best flowfield results are obtained when $\sigma = 1$ is used. Fig. 1 shows the convergence histories using $\sigma = 1$ and adaptive σ

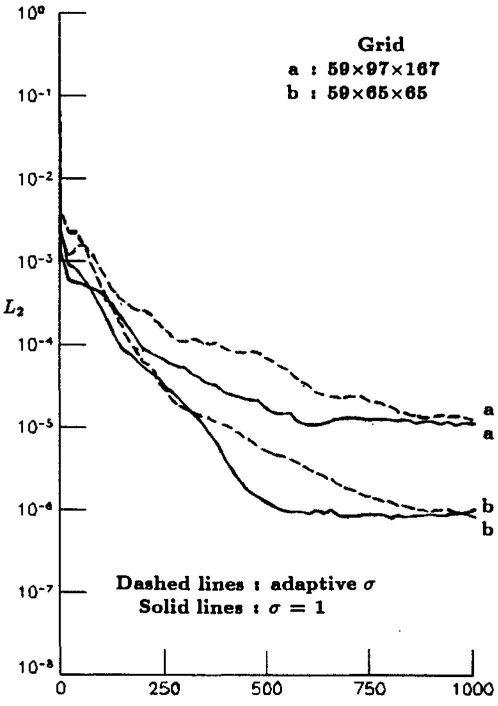

Fig. 1 Numerical convergence for the double-delta wing; $\alpha = 12$ deg, $Re = 1.3 \times 10^6$ ($\gamma = -1$).

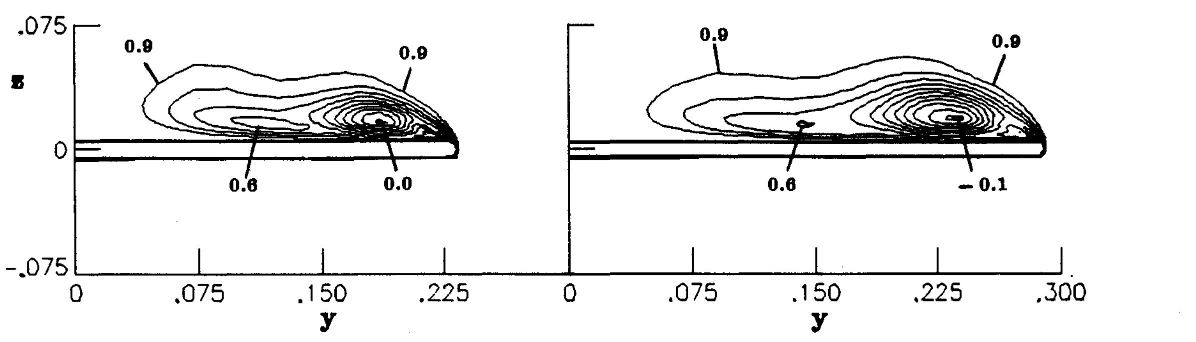

a) x = 0.75

b) x = 0.85

Fig. 2 Total pressure coefficient contours for the double-delta wing using 59 × 65 × 65 grid; $\alpha = 12$ deg, $Re = 1.3 \times 10^6$ ($\gamma = -1$ and $\sigma = 1$).

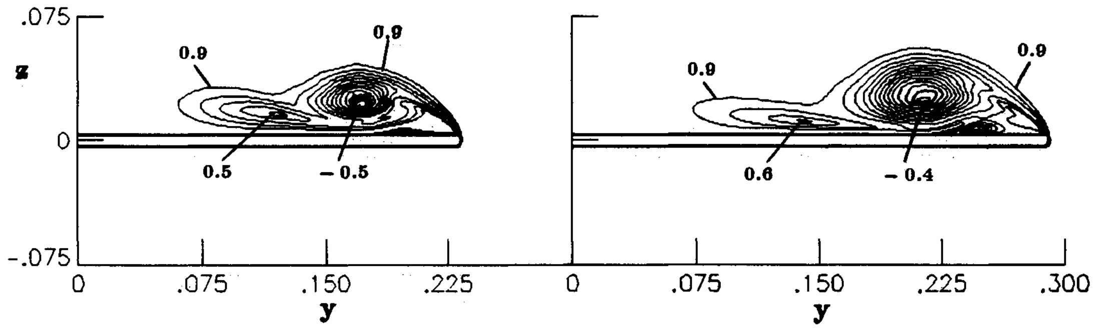

a) x = 0.75 b) x = 0.85

Fig. 3 Total pressure coefficient contours for the double-delta wing using 59 × 97 × 167 grid; α = 12 deg, Re = 1.3 × 10^6 (γ = −1 and σ = 1).

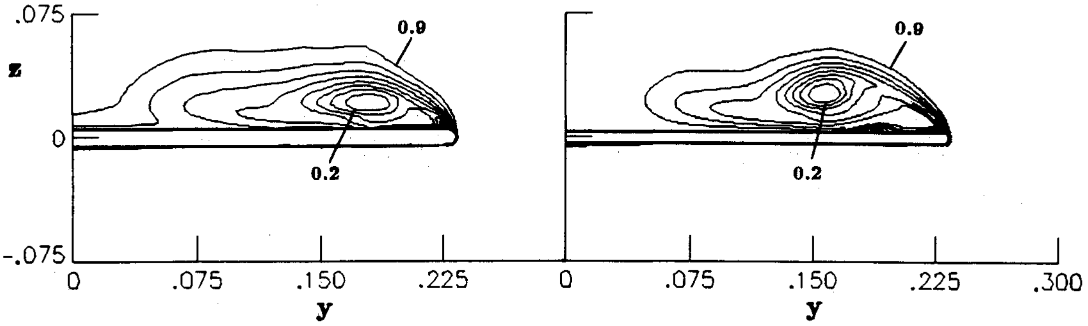

a) Grid : 59x65x65 b) Grid : 59x97x167

Fig. 4 Total pressure coefficient contours at x = 0.75 for the double-delta wing using adaptive σ; α = 12 deg, Re = 1.3 × 10^6 (γ = −1).

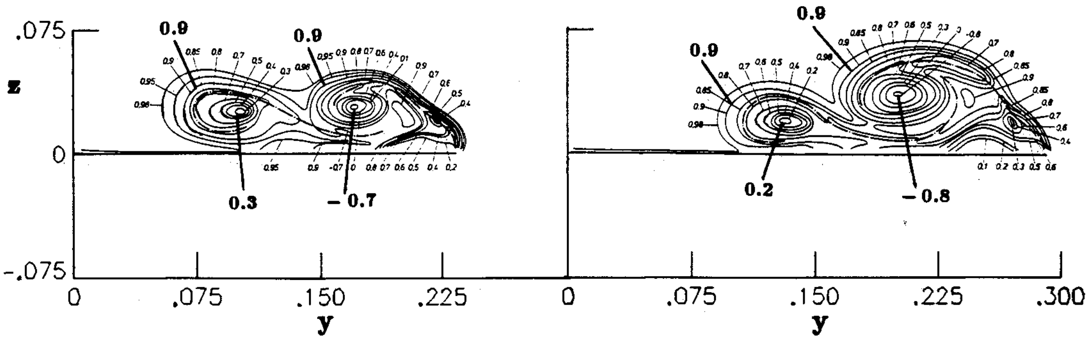

a) x = 0.75 b) x = 0.85

Fig. 5 Experimental[16] total pressure coefficient contours for the double-delta wing; α = 12 deg, Re = 1.3 × 10^6.

with $\gamma = -1$ for the fine (59 × 97 × 167) and coarse (59 × 65 × 65) grids, where L_2 norm represents the square root of the sum of the square of residuals for all primitive variables. For the same grid, the convergence rate with $\sigma = 1$ (solid lines) is slightly better than that with adaptive σ (dashed lines). As the grid is refined, the convergence rate deteriorates. One of the possible causes is that large local residuals may be resulted from large local truncation errors at mathematical singularities such as near the apex, the leading edge, and the trailing edge, where highly stretched grid sizes have been used to resolve large local flow gradients.

Constant contours of computed total pressure coefficients C_t are displayed in Figs. 2–5, where $\Delta C_t = 0.1$ is chosen for the neighboring contours. For the coarse-grid computations, at $x = 0.75$ (all length scales are normalized by c unless otherwise specified), both the strake (inboard) and the corotating wing (outboard) vortices are clearly seen in Fig. 2a. At $x = 0.85$ the two primary vortices start merging into one vortex as shown in Fig. 2b. It should be noted that the previous results[17,18] using a singular eigensystem fail to resolve the strake vortex for the same coarse grid. Therefore, better numerical accuracy has been obtained using the nonsingular eigensystem, which results in less truncation errors.

Figures 3a and 3b exhibit constant contours of C_t for the fine grid. At both $x = 0.75$ (Fig. 3a) and $x = 0.85$ (Fig. 3b), the two primary vortices are better resolved in the sense of clearer and tighter vortical cores as compared to their coarse-grid counterparts. Also, a distinct counter-rotating secondary vortex is observed underneath the primary wing vortex at each cross plane. For the fine grid, the present results show only slightly better flow resolution than the previous corresponding results.[17,18] This is probably because of higher rounding errors in fine-grid computations and loss of accuracy due to severe grid stretching.

The effect of adaptive σ with $\gamma = -1$ on total pressure coefficient contours at $x = 0.75$ is shown in Figs. 4a and 4b. The strake vortex is not resolved and the wing vortex is very diffusive for both the coarse (Fig. 4a) and fine (Fig. 4b) grids. It is apparent that hefty numerical damping has resulted from the present upwind-relaxation scheme when the adaptive σ is used.

Available experimental contours[16] of C_t at $x = 0.75$ and $x = 0.85$ are displayed in Figs. 5a and 5b for comparison. At the two cross planes, both the primary strake and wing vortices are clearly observed, but the secondary vortices are not seen, owing to experimental difficulties. Comparison of Fig.

Table 1 Double-delta wing; α = 12 deg, $Re = 1.3 \times 10^6$ ($\gamma = -1$)

σ	Grid	$(C_t)_s$	$(C_t)_w$	y_s	z_s	y_w	z_w	C_L
Adaptive	59 × 65 × 65		0.2			0.181	0.021	0.507
1	59 × 65 × 65	0.6	0.0	0.121	0.016	0.186	0.018	0.499
Adaptive	59 × 97 × 167		0.2			0.159	0.026	0.521
1	59 × 97 × 167	0.5	−0.5	0.120	0.018	0.171	0.024	0.522
Brennenstuhl and Hummel's data[16]		0.3	−0.7	0.103	0.024	0.171	0.028	0.525

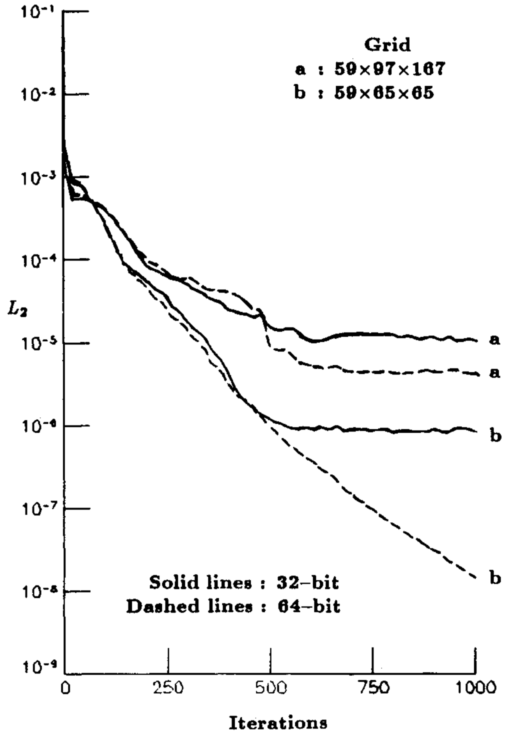

Fig. 6 Effect of machine accuracy on the numerical convergence for the double-delta wing; α = 12 deg, $Re = 1.3 \times 10^6$ ($\gamma = -1$ and $\sigma = 1$).

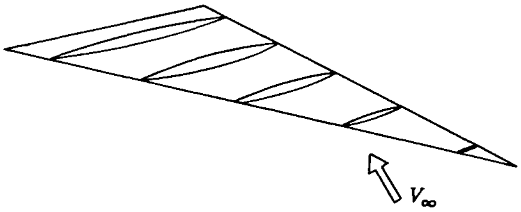

Fig. 7 Biconvex delta wing geometry.

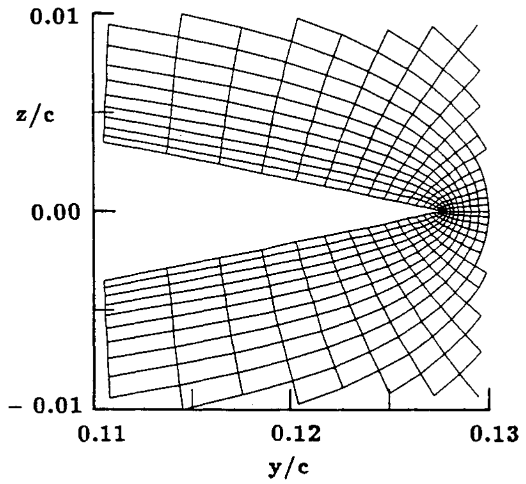

Fig. 8 Elliptic grid near the leading edge of the delta wing; $x = 0.5$.

4 with Fig. 5 indicates that numerical results using the adaptive σ are too diffusive to resolve the vortical flowfields. For $\sigma = 1$, quantitatively (qualitatively) good agreement in C_t is obtained for the fine (coarse) grid as seen from the comparison of Fig. 5 with Fig. 3 (Fig. 2).

A summary of quantitative comparisons is given in Table 1, where $(C_t)_s$ and $(C_t)_w$ are the minimum values of C_t at $x = 0.75$ for the strake and wing vortices, respectively; (y_s, z_s) and (y_w, z_w) stand for lateral and vertical positions of the vortical cores at $x = 0.75$ for the strake and wing vortices, respectively; and C_L is the lift coefficient. Computational results using adaptive σ fail to predict the strake vortex for both the coarse and fine grids. In lack of resolution, the coarse-grid results using $\sigma = 1$ yield much higher level of $(C_t)_w$, predict the position of the wing-vortex core further outboard and much closer to the wing upper surface, and underpredict C_L. On the other hand, the fine-grid results using $\sigma = 1$ predict $(C_t)_w$ much better and give excellent agreements in the position of the wing-vortex core and C_L. However, both the coarse- and fine-grid results suggest that the position of the strake-vortex core is predicted more outboard and closer to the upper wing surface.

The effect of machine accuracy on the convergence for the double-delta wing is shown in Fig. 6. For the coarse grid, L_2 norm can be further reduced by about two orders of magnitude for the 64-bit computations as compared to the 32-bit computations. For the fine grid, however, the further reduction in L_2 norm using 64-bit arithmetic is only half order of magnitude. Also, the flowfield results indicate no significant changes by using higher machine accuracy.[11]

Sideslipping Delta Wing

The sharp-edged delta wing has a leading-edge sweep of 76 deg. The cross sections perpendicular to the root chord of the wing are circular biconvex as shown in Fig. 7. The maximum thickness is 3.2% of c at $x \approx 0.7$. This geometry was carefully tested in a low-speed ($M_\infty \approx 0.1$) wind tunnel at $Re = 2.5 \times 10^6$ and well documented.[19,20]

A single H–O grid consisting of 51 successive crossplanes is generated. Longitudinally, there are 10, 30, and 11 cross planes upstream of the apex, on the wing, and in the wake, respectively. The origin of the coordinate system is located at the apex of the wing. Each cross-plane grid is obtained by solving two Poisson equations. There are 73 and 217 grid points in the radial and circumferential directions, respectively. A detailed grid near the leading edge at $x = 0.5$ is shown in Fig. 8. The computational domain extends one root chord ahead of the apex, one and one-half root chords in the wake, and about two root chords away from the longitudinal axis of the wing.

The case computed with 32-bit word arithmetic is for flow conditions of α = 21 deg, 0 deg $\le \beta \le$ 20 deg, and $Re = 2.5 \times 10^6$. The turbulent modeling is used in this case. The law-of-the-wall coordinate y^+ at the first grid point off the wing surface is about 5. Since the flowfield is not symmetric with respect to the longitudinal plane of symmetry (root-chord plane), the full flowfield over the complete wing is computed. Reflection conditions are not applied on the plane of symmetry. In computations, there is a branch cut for the H–O grid of the wing. It is set at the geometrically symmetric plane underneath the wing surface. The flowfield values along the

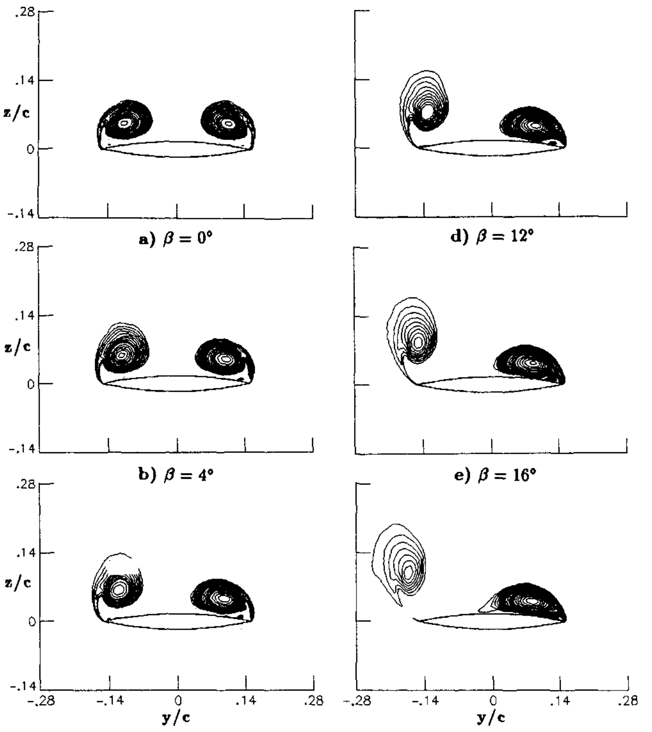

a) $\beta = 0°$ b) $\beta = 4°$ c) $\beta = 8°$ d) $\beta = 12°$ e) $\beta = 16°$ f) $\beta = 20°$

Fig. 9 **Computed total pressure coefficient contours for the sideslipping delta wing; $x = 0.6$, $\alpha = 21$ deg, $Re = 2.5 \times 10^6$ ($\gamma = -1$, $\sigma = 1$).**

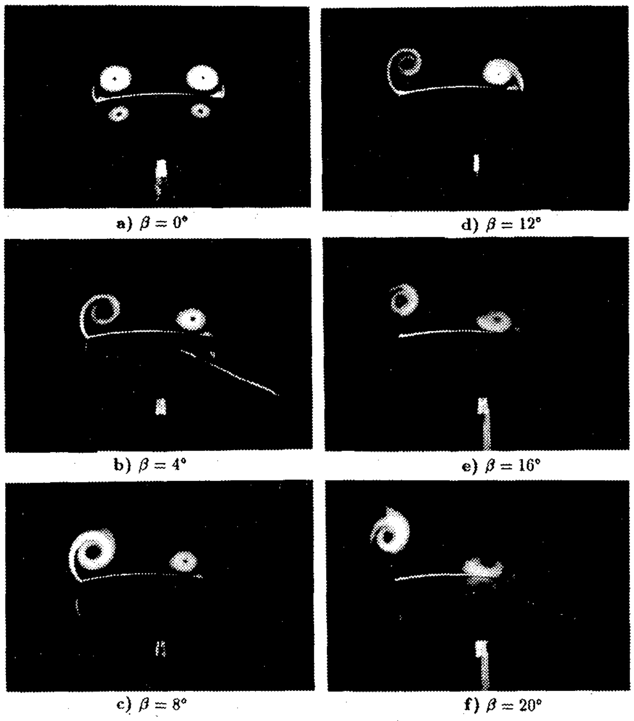

a) $\beta = 0°$ b) $\beta = 4°$ c) $\beta = 8°$ d) $\beta = 12°$ e) $\beta = 16°$ f) $\beta = 20°$

Fig. 10 **Vortex flow visualization of the sideslipping delta wing using smoke/laser light sheet technique[19]; $x = 0.6$, $\alpha = 21$ deg, $Re = 2.5 \times 10^6$.**

branch cut are simply computed as averages from the interior neighboring points. Since the best numerical convergence and most accurate results are obtained by using $\gamma = -1$ and $\sigma = 1$,[11] these two values are used in this case.

Computed total pressure coefficient contours are shown in Figs. 9a through 9f to illustrate the effect of angle of sideslip on the vortical flow structures at $x = 0.6$. With increasing sideslip the windward leading-edge vortex moves inboard and closer to the upper surface of the wing, while the leeward leading-edge vortex moves outboard and away from the wing surface. The vortical core of the leeward vortex moves outboard of the wing at angles of sideslip beyond 16 deg. In addition, under the windward vortex, a secondary vortex is visible very close to the wing surface for $\beta \geq 4$ deg. Corresponding crossflow vortex flows obtained by smoke/laser light sheet technique[19] are shown in Figs. 10a through 10f. Close similarity is demonstrated.

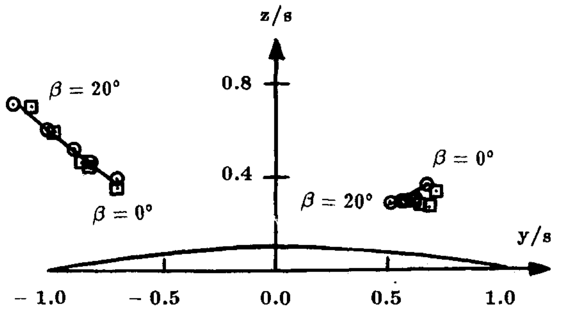

Fig. 11 **Vortex core positions for the sideslipping delta wing; $x = 0.6$, $\alpha = 21$ deg, $Re = 2.5 \times 10^6$. ——, Present computations; ⊙, Kiel probe measurements[19]; ⊡, smoke/laser light sheet measurements.[19]**

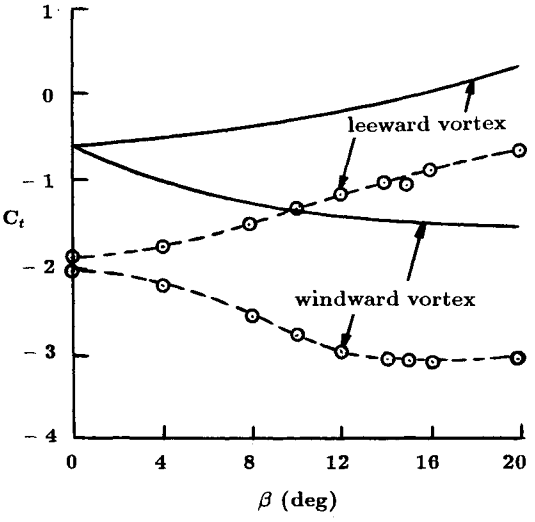

Fig. 12 **Total pressure coefficients at vortical cores for the sideslipping delta wing; $x = 0.6$, $\alpha = 21$ deg, $Re = 2.5 \times 10^6$. ——, Present computations; ⊙, Kiel probe measurements.[19]**

Computed positions of local total pressure minima (solid lines) are compared with both Kiel probe (circles) and smoke/laser light sheet (squares) measurements[19] of vortex core positions in Fig. 11, where s is the local wing semispan. The numerical variation of vortex core positions with angles of sideslip is in good agreement with both measurements for the leeward vortex, but it agrees better with Kiel probe data than with smoke/laser light sheet data for the windward vortex.

Computed total pressure coefficients in vortical cores at $x = 0.6$ are compared with Kiel probe measurements[19] in Fig. 12. Numerical results indicate that with increasing sideslip the total pressure coefficient in vortical core increases (decreasing vortical strength) for the leeward vortex and decreases (increasing vortical strength) for the windward vortex. The variation of minimum total pressure coefficient in sideslip is similar to the experimental trend, but the vortical strengths are underpredicted. This points out that a much finer grid near the vortical core or a higher-order numerical scheme is required to fully resolve the large flow gradient near the viscous vortex core. Furthermore, since boundary layer transition depends on α, β, and Re,[19,20] a turbulence model capable of predicting transitional flows must be exploited.

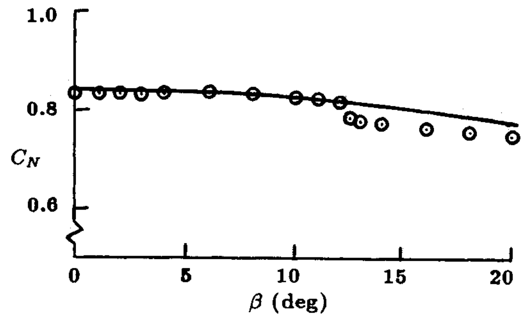

a) Normal force

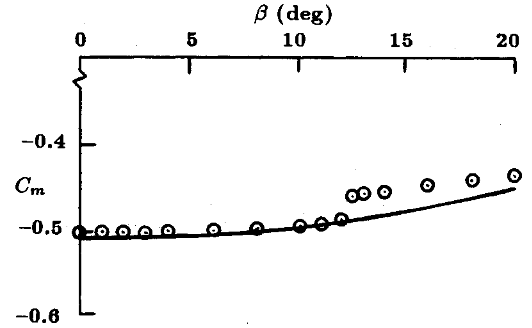

b) Pitching moment

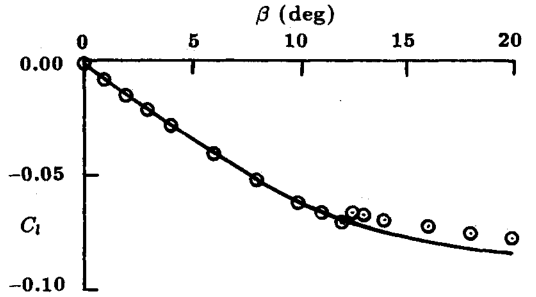

c) Rolling moment

Fig. 13 Force and moment coefficients for the sideslipping delta wing; $\alpha = 21$ deg, $Re = 2.5 \times 10^6$. ——, Present computations; ⊙, balance measurements.[20]

In Fig. 13, the variations with angles of sideslip for the normal force C_N, the pitching moment coefficient C_m (referred to the apex of the wing), and the rolling moment coefficient C_l are shown. With increasing sideslip, C_N decreases, C_m increases, and C_l decreases gradually. Up to $\beta = 12$ deg, the agreement with balance measurements[20] is excellent. However, numerical results fail to predict the sharp change in the force and moment curves between $\beta = 12$ deg and 12.5 deg, where vortex breakdown initiates near the trailing edge of the wing in the experiment.[19,20] Also, slight deviation occurs for $\beta > 12$ deg.

Conclusions

The time-iterative method using the preconditioned nonsingular eigensystem has been implemented to obtain steady-state Navier-Stokes solutions for the flows past a round-edged double-delta wing and a sharp-edged delta wing. The best numerical convergence and most accurate results are achieved when $\gamma = -1$ and $\sigma = 1$ are used. In other words, the artificial compressibility approach with $\sigma = 1$ gives the optimum preconditioned system of equations. Good agreement with measured data is shown for force and moment coefficients as well as vortex core positions. However, the vortical strength is underpredicted for lack of grid resolution in the neighborhood of vortical cores.

Appendix: Three-Dimensional Eigensystem

The right R and left L eigenvectors of the modified inviscid-flux Jacobians A_i are derived in the following. For simplicity the subscript i will be dropped here. The right eigenvector is

$$R = [\boldsymbol{R}_1\ \boldsymbol{R}_2\ \boldsymbol{R}_3\ \boldsymbol{R}_4]$$
$$= \begin{bmatrix} S^+\lambda^+ & 0 & 0 & -S^-\lambda^- \\ -\gamma u - a\lambda^+ & O & X & -\gamma u - a\lambda^- \\ -\gamma v - b\lambda^+ & P & Y & -\gamma v - b\lambda^- \\ -\gamma w - c\lambda^+ & Q & Z & -\gamma w - c\lambda^- \end{bmatrix} \tag{A1}$$

where

$$S^+ = S + \frac{1}{2}(1 + \gamma)U$$
$$S^- = S - \frac{1}{2}(1 + \gamma)U$$
$$O = -(ab + c^2)$$
$$P = a^2 - bc$$
$$Q = ac + b^2$$
$$X = -a^2c + abc + b^3 + bc^2$$
$$Y = -a^2c - ab^2 - abc - c^3$$
$$Z = a^3 + ab^2 - abc + bc^2$$

$\boldsymbol{R}_1$ and $\boldsymbol{R}_4$ are constructed through $\lambda_1 = \lambda^-$ and $\lambda_4 = \lambda^+$, respectively. Since $\lambda_2 = \lambda_3 = U$, the corresponding vectors $\boldsymbol{R}_2$ and $\boldsymbol{R}_3$ must be carefully chosen to be unparalleled so that the $det[R]$ will not be zero. If a, b, and c are not all zeros, one can assume

$$\nabla R_0 = ai + bj + ck$$
$$\boldsymbol{R}_2 = Oi + Pj + Qk$$
$$\boldsymbol{R}_3 = Xi + Yj + Zk$$
$$\boldsymbol{R}_5 = -bi + cj - ak$$

where $\boldsymbol{R}_5$ can be any arbitrary vector as long as it is a nontrivial one. Now, $\boldsymbol{R}_2$ and $\boldsymbol{R}_3$ can be chosen as

$$\boldsymbol{R}_2 = \nabla R_0 \times \boldsymbol{R}_5 \neq 0$$
$$\boldsymbol{R}_3 = \nabla R_0 \times \boldsymbol{R}_2 \neq 0$$

then

$$\nabla R_0 \cdot \boldsymbol{R}_2 = 0$$
$$\nabla R_0 \cdot \boldsymbol{R}_3 = 0$$

are automatically satisfied. Consequently, $\boldsymbol{R}_1$, $\boldsymbol{R}_2$, $\boldsymbol{R}_3$, and $\boldsymbol{R}_4$ are linearly independent vectors, and the right eigenvector is nonsingular.

The left eigenvector is

$$L = \frac{1}{det[R]} L_{ij} \tag{A2}$$

where

$$
\begin{aligned}
det[R] &= 2KS^{-}\,SS^{+}\\
K &= O^2 + P^2 + Q^2\\
L_{11} &= KS^{-}\\
L_{12} &= aKS^{-}\lambda^{-}\\
L_{13} &= bKS^{-}\lambda^{-}\\
L_{14} &= cKS^{-}\lambda^{-}\\
L_{21} &= 2\gamma S[X(bw - cv) + Y(cu - aw) + Z(av - bu)]\\
L_{22} &= 2S(Y(\sigma c - \gamma wU) - Z(\sigma b - \gamma vU)]\\
L_{23} &= 2S[Z(\sigma a - \gamma uU) - X(\sigma c - \gamma wU)]\\
L_{24} &= 2S[X(\sigma b - \gamma vU) - Y(\sigma a - \gamma uU)]\\
L_{31} &= -2\gamma S[O(bw - cv) + P(cu - aw)\\
&\quad + Q(av - bu)]\\
L_{32} &= -2S[P(\sigma c - \gamma wU) - Q(\sigma b - \gamma vU)]\\
L_{33} &= -2S[Q(\sigma a - \gamma uU) - O(\sigma c - \gamma wU)]\\
L_{34} &= -2S[O(\sigma b - \gamma vU) - P(\sigma a - \gamma uU)]\\
L_{41} &= KS^{+}\\
L_{42} &= aKS^{+}\lambda^{+}\\
L_{43} &= bKS^{+}\lambda^{+}\\
L_{44} &= cKS^{+}\lambda^{+}
\end{aligned}
$$

Since $K \neq 0$, the left eigenvector is also nonsingular.

Acknowledgment

The work of the first author was supported by the NASA Langley Research Center under Contract NAS1-18585.

References

[1] Turkel, E., "Preconditioned Methods for Solving the Incompressible and Low Speed Compressible Equations," *Journal of Computational Physics*, Vol. 72, No. 2, 1987, pp. 277–298.

[2] Steger, J. L., and Kutler, P., "Implicit Finite-Difference Procedures for the Computation of Vortex Wakes," *AIAA Journal*, Vol. 15, April 1977, pp. 581–590.

[3] Feng, J., and Merkle, C. L., "Evaluation of Preconditioning Methods for Time-Marching Systems," AIAA Paper 90-0016, Reno, NV, Jan. 1990.

[4] Chorin, A. J., "A Numerical Method for Solving Incompressible Viscous Flow Problems," *Journal of Computational Physics*, Vol. 2, No. 1, 1967, pp. 12–26.

[5] Rizzi, A., and Eriksson, L.-E., "Computation of Inviscid Incompressible Flow with Rotation," *Journal of Fluid Mechanics*, Vol. 153, April, 1985, pp. 275–312.

[6] Kwak, D., Chang, J. C. L., Shanks, S. P., and Chakravarthy, S. R., "An Incompressible Navier-Stokes Flow Solver in Three-Dimensional Curvilinear Coordinate System Using Primitive Variables," *AIAA Journal*, Vol. 24, March 1986, pp. 390–396.

[7] Hsu, C.-H., Hartwich, P.-M., and Liu, C. H., "Computation of Vortical Interaction for a Sharp-Edged Double-Delta Wing," *Journal of Aircraft*, Vol. 25, May 1988, pp. 442–447.

[8] Hartwich, P.-M., and Hsu, C.-H., "High Resolution Upwind Schemes for the Three-Dimensional Incompressible Navier-Stokes Equations," *AIAA Journal*, Vol. 26, Nov. 1988, pp. 1321–1328.

[9] Rogers, S. E., Kwak, D., and Kris, C., "Numerical Solution of the Incompressible Navier-Stokes Equations for Steady-State and Time-Dependent Problems," AIAA Paper 89-0463, Reno, NV, Jan. 1989.

[10] Pan, D., and Chakravarthy, S., "Unified Formulation for Incompressible Flows," AIAA Paper 89-0122, Reno, NV, Jan. 1989.

[11] Hus, C.-H., Chen, Y.-M., and Liu, C. H., "Preconditioned Upwind Methods to Solve 3-D Incompressible Navier-Stokes Equations for Viscous Flows," AIAA Paper 90-1496, Seattle, WA, June 1990.

[12] Roe, P. L., "Approximate Rieman Solvers, Parameter Vectors, and Difference Schemes," *Journal of Computational Physics*, Vol. 43, No. 2, 1981, pp. 357–372.

[13] Yee, H. C., Warming, R. F., and Harten, A., "Implicit Total Variation Diminishing (TVD) Schemes for Steady-State Calculations," *Journal of Computational Physics*, Vol. 57, No. 3, 1985, pp. 327–360.

[14] Baldwin, B. S., and Lomax, H., "Thin Layer Approximation and Algebraic Model for Separated Turbulent Flows," AIAA Paper 78-257, Huntsville, AL, Jan. 1978.

[15] Degani, D., and Schiff, L. B., "Computation of Turbulent Supersonic Flows around Pointed Bodies Having Crossflow Separation," *Journal of Computational Physics*, Vol. 66, No. 1, 1986, pp. 173–196.

[16] Brennenstuhl, U., and Hummel, D., "Vortex Formation over Double-Delta Wings," International Council of the Aeronautical Sciences Paper 82-6. 6. 3, Seattle, WA, Aug. 1982.

[17] Hsu, C.-H., and Liu, C. H., "Navier-Stokes Computation of Flow around a Round-Edged Double-Delta Wing," *AIAA Journal*, Vol. 28, June 1990, pp. 961–968.

[18] Hsu, C.-H., and Liu, C. H., "Simulation of Leading-Edge Vortex Flows," *Theoretical and Computational Fluid Dynamics*, Vol. 1, July–Aug. 1990, pp. 379–390.

[19] Naarding, S. H. J., and Verhaagen, N. G., "Experimental and Numerical Investigation of the Vortex Flow over a Sharp Edged Delta Wing; with and without Sideslip," Delft Univ. of Technology, Deft, The Netherlands, Rept. LR-573, Dec. 1988.

[20] Verhaagen, N. G., and Naarding, S. H. J., "Experimental and Numerical Investigation of Vortex Flow over a Sideslipping Delta Wing," *Journal of Aircraft*, Vol. 26, Nov., 1989, pp. 971–978.